

# Dark Energy Survey Year 1 Results: Cross-correlation between DES Y1 galaxy weak lensing and SPT+*Planck* CMB weak lensing

Y. Omori,<sup>1,2,3</sup> E. J. Baxter,<sup>4</sup> C. Chang,<sup>5</sup> D. Kirk,<sup>6</sup> A. Alarcon,<sup>7,8</sup> G. M. Bernstein,<sup>4</sup> L. E. Bleem,<sup>9,5</sup> R. Cawthon,<sup>5</sup> A. Choi,<sup>10</sup> R. Chown,<sup>11,3</sup> T. M. Crawford,<sup>5,12</sup> C. Davis,<sup>1</sup> J. De Vicente,<sup>13</sup> J. DeRose,<sup>1,2</sup> S. Dodelson,<sup>14</sup> T. F. Eifler,<sup>15,16</sup> P. Fosalba,<sup>7,8</sup> O. Friedrich,<sup>17,18</sup> M. Gatti,<sup>19</sup> E. Gaztanaga,<sup>7,8</sup> T. Giannantonio,<sup>20,21,18</sup> D. Gruen,<sup>1,22</sup> W. G. Hartley,<sup>6,23</sup> G. P. Holder,<sup>3,24,25,26</sup> B. Hoyle,<sup>17,18</sup> D. Huterer,<sup>27</sup> B. Jain,<sup>4</sup> M. Jarvis,<sup>4</sup> E. Krause,<sup>15</sup> N. MacCrann,<sup>10,28</sup> R. Miquel,<sup>29,19</sup> J. Prat,<sup>19</sup> M. M. Rau,<sup>14,18</sup> C. L. Reichardt,<sup>30</sup> E. Rozo,<sup>31</sup> S. Samuroff,<sup>14</sup> C. Sánchez,<sup>4,19</sup> L. F. Secco,<sup>4</sup> E. Sheldon,<sup>32</sup> G. Simard,<sup>3</sup> M. A. Troxel,<sup>10,28</sup> P. Vielzeuf,<sup>19</sup> R. H. Wechsler,<sup>1,2,22</sup> J. Zuntz,<sup>33</sup> T. M. C. Abbott,<sup>34</sup> F. B. Abdalla,<sup>6,35</sup> S. Allam,<sup>36</sup> J. Annis,<sup>36</sup> S. Avila,<sup>37</sup> K. Aylor,<sup>38</sup> B. A. Benson,<sup>5,12,36</sup> E. Bertin,<sup>39,40</sup> S. L. Bridle,<sup>41</sup> D. Brooks,<sup>6</sup> D. L. Burke,<sup>1,22</sup> J. E. Carlstrom,<sup>5,9,12,42,43</sup> A. Carnero Rosell,<sup>44,45</sup> M. Carrasco Kind,<sup>25,46</sup> J. Carretero,<sup>19</sup> F. J. Castander,<sup>7,8</sup> C. L. Chang,<sup>9,5,12</sup> H.-M. Cho,<sup>22</sup> A. T. Crites,<sup>47</sup> M. Crocce,<sup>7,8</sup> C. E. Cunha,<sup>1</sup> L. N. da Costa,<sup>44,45</sup> T. de Haan,<sup>48,49</sup> S. Desai,<sup>50</sup> H. T. Diehl,<sup>36</sup> J. P. Dietrich,<sup>51,52</sup> M. A. Dobbs,<sup>3,53</sup> W. B. Everett,<sup>54</sup> E. Fernandez,<sup>19</sup> B. Flaugher,<sup>36</sup> J. Frieman,<sup>36,5</sup> J. García-Bellido,<sup>55</sup> E. M. George,<sup>48,56</sup> R. A. Gruendl,<sup>25,46</sup> G. Gutierrez,<sup>36</sup> N. W. Halverson,<sup>54,57</sup> N. L. Harrington,<sup>48</sup> D. L. Hollowood,<sup>58</sup> K. Honscheid,<sup>10,28</sup> W. L. Holzapfel,<sup>48</sup> Z. Hou,<sup>5,12</sup> J. D. Hrubes,<sup>59</sup> D. J. James,<sup>60</sup> T. Jeltema,<sup>58</sup> K. Kuehn,<sup>61</sup> N. Kuropatkin,<sup>36</sup> M. Lima,<sup>62,44</sup> H. Lin,<sup>36</sup> A. T. Lee,<sup>48,49</sup> E. M. Leitch,<sup>5,12</sup> D. Luong-Van,<sup>59</sup> M. A. G. Maia,<sup>44,45</sup> A. Manzotti,<sup>63,5,12</sup> D. P. Marrone,<sup>64</sup> J. L. Marshall,<sup>65</sup> P. Martini,<sup>10,66</sup> J. J. McMahon,<sup>27</sup> P. Melchior,<sup>67</sup> F. Menanteau,<sup>25,46</sup> S. S. Meyer,<sup>5,12,43,68</sup> L. M. Mocz,<sup>5,12</sup> J. J. Mohr,<sup>51,52,17</sup> T. Natoli,<sup>5,42,69</sup> R. L. C. Ogando,<sup>44,45</sup> S. Padin,<sup>5,12</sup> A. A. Plazas,<sup>16</sup> C. Pryke,<sup>70</sup> A. K. Romer,<sup>71</sup> A. Roodman,<sup>1,22</sup> J. E. Ruhl,<sup>72</sup> E. S. Rykoff,<sup>1,22</sup> E. Sanchez,<sup>13</sup> V. Scarpine,<sup>36</sup> K. K. Schaffer,<sup>5,43,73</sup> R. Schindler,<sup>22</sup> I. Sevilla-Noarbe,<sup>13</sup> E. Shirokoff,<sup>48,5,12</sup> M. Smith,<sup>74</sup> R. C. Smith,<sup>34</sup> M. Soares-Santos,<sup>75</sup> F. Sobreira,<sup>76,44</sup> Z. Staniszewski,<sup>72,16</sup> A. A. Stark,<sup>60</sup> K. T. Story,<sup>1,77</sup> E. Suchyta,<sup>78</sup> M. E. C. Swanson,<sup>46</sup> G. Tarle,<sup>27</sup> D. Thomas,<sup>37</sup> K. Vanderlinde,<sup>69,79</sup> J. D. Vieira,<sup>25,26</sup> V. Vikram,<sup>80</sup> A. R. Walker,<sup>34</sup> J. Weller,<sup>51,17,18</sup> R. Williamson,<sup>5,12</sup> W. L. K. Wu,<sup>5</sup> and O. Zahn<sup>81</sup>

(DES & SPT Collaborations)

<sup>1</sup>Kavli Institute for Particle Astrophysics & Cosmology,

P. O. Box 2450, Stanford University, Stanford, CA 94305, USA

<sup>2</sup>Department of Physics, Stanford University, 382 Via Pueblo Mall, Stanford, CA 94305, USA

<sup>3</sup>Department of Physics and McGill Space Institute, McGill University, Montreal, Quebec H3A 2T8, Canada

<sup>4</sup>Department of Physics and Astronomy, University of Pennsylvania, Philadelphia, PA 19104, USA

<sup>5</sup>Kavli Institute for Cosmological Physics, University of Chicago, Chicago, IL 60637, USA

<sup>6</sup>Department of Physics & Astronomy, University College London, Gower Street, London, WC1E 6BT, UK

<sup>7</sup>Institut d'Estudis Espacials de Catalunya (IEEC), 08193 Barcelona, Spain

<sup>8</sup>Institute of Space Sciences (ICE, CSIC), Campus UAB,

Carrer de Can Magrans, s/n, 08193 Barcelona, Spain

<sup>9</sup>High Energy Physics Division, Argonne National Laboratory, Argonne, IL, USA 60439

<sup>10</sup>Center for Cosmology and Astro-Particle Physics, The Ohio State University, Columbus, OH 43210, USA

<sup>11</sup>Department of Physics and Astronomy, McMaster University,

1280 Main St. W., Hamilton, ON L8S 4L8, Canada

<sup>12</sup>Department of Astronomy and Astrophysics, University of Chicago, Chicago, IL 60637, USA

<sup>13</sup>Centro de Investigaciones Energéticas, Medioambientales y Tecnológicas (CIEMAT), Madrid, Spain

<sup>14</sup>Department of Physics, Carnegie Mellon University, Pittsburgh, Pennsylvania 15312, USA

<sup>15</sup>Department of Astronomy/Steward Observatory, 933 North Cherry Avenue, Tucson, AZ 85721-0065, USA

<sup>16</sup>Jet Propulsion Laboratory, California Institute of Technology, 4800 Oak Grove Dr., Pasadena, CA 91109, USA

<sup>17</sup>Max Planck Institute for Extraterrestrial Physics, Giessenbachstrasse, 85748 Garching, Germany

<sup>18</sup>Universitäts-Sternwarte, Fakultät für Physik, Ludwig-Maximilians Universität München, Scheinerstr. 1, 81679 München, Germany

<sup>19</sup>Institut de Física d'Altes Energies (IFAE), The Barcelona Institute of

Science and Technology, Campus UAB, 08193 Bellaterra (Barcelona) Spain

<sup>20</sup>Institute of Astronomy, University of Cambridge, Madingley Road, Cambridge CB3 0HA, UK

<sup>21</sup>Kavli Institute for Cosmology, University of Cambridge, Madingley Road, Cambridge CB3 0HA, UK

<sup>22</sup>SLAC National Accelerator Laboratory, Menlo Park, CA 94025, USA

<sup>23</sup>Department of Physics, ETH Zurich, Wolfgang-Pauli-Strasse 16, CH-8093 Zurich, Switzerland

<sup>24</sup>Canadian Institute for Advanced Research, CIFAR Program in Cosmology and Gravity, Toronto, ON, M5G 1Z8, Canada

<sup>25</sup>Department of Astronomy, University of Illinois at Urbana-Champaign, 1002 W. Green Street, Urbana, IL 61801, USA

<sup>26</sup>Department of Physics, University of Illinois Urbana-Champaign, 1110 W. Green Street, Urbana, IL 61801, USA

<sup>27</sup>Department of Physics, University of Michigan, Ann Arbor, MI 48109, USA

<sup>28</sup>Department of Physics, The Ohio State University, Columbus, OH 43210, USA

<sup>29</sup>Institució Catalana de Recerca i Estudis Avançats, E-08010 Barcelona, Spain

<sup>30</sup>School of Physics, University of Melbourne, Parkville, VIC 3010, Australia

<sup>31</sup>Department of Physics, University of Arizona, Tucson, AZ 85721, USA

<sup>32</sup>Brookhaven National Laboratory, Bldg 510, Upton, NY 11973, USA

- <sup>33</sup>*Institute for Astronomy, University of Edinburgh, Edinburgh EH9 3HJ, UK*
- <sup>34</sup>*Cerro Tololo Inter-American Observatory, National Optical Astronomy Observatory, Casilla 603, La Serena, Chile*
- <sup>35</sup>*Department of Physics and Electronics, Rhodes University, PO Box 94, Grahamstown, 6140, South Africa*
- <sup>36</sup>*Fermi National Accelerator Laboratory, P. O. Box 500, Batavia, IL 60510, USA*
- <sup>37</sup>*Institute of Cosmology & Gravitation, University of Portsmouth, Portsmouth, PO1 3FX, UK*
- <sup>38</sup>*Department of Physics, University of California, Davis, CA, USA 95616*
- <sup>39</sup>*CNRS, UMR 7095, Institut d'Astrophysique de Paris, F-75014, Paris, France*
- <sup>40</sup>*Sorbonne Universités, UPMC Univ Paris 06, UMR 7095, Institut d'Astrophysique de Paris, F-75014, Paris, France*
- <sup>41</sup>*Jodrell Bank Center for Astrophysics, School of Physics and Astronomy, University of Manchester, Oxford Road, Manchester, M13 9PL, UK*
- <sup>42</sup>*Department of Physics, University of Chicago, Chicago, IL 60637, USA*
- <sup>43</sup>*Enrico Fermi Institute, University of Chicago, Chicago, IL 60637, USA*
- <sup>44</sup>*Laboratório Interinstitucional de e-Astronomia - LIneA, Rua Gal. José Cristino 77, Rio de Janeiro, RJ - 20921-400, Brazil*
- <sup>45</sup>*Observatório Nacional, Rua Gal. José Cristino 77, Rio de Janeiro, RJ - 20921-400, Brazil*
- <sup>46</sup>*National Center for Supercomputing Applications, 1205 West Clark St., Urbana, IL 61801, USA*
- <sup>47</sup>*California Institute of Technology, Pasadena, CA, USA 91125*
- <sup>48</sup>*Department of Physics, University of California, Berkeley, CA, USA 94720*
- <sup>49</sup>*Physics Division, Lawrence Berkeley National Laboratory, Berkeley, CA, USA 94720*
- <sup>50</sup>*Department of Physics, IIT Hyderabad, Kandi, Telangana 502285, India*
- <sup>51</sup>*Excellence Cluster Universe, Boltzmannstr. 2, 85748 Garching, Germany*
- <sup>52</sup>*Faculty of Physics, Ludwig-Maximilians-Universität, Scheinerstr. 1, 81679 Munich, Germany*
- <sup>53</sup>*Canadian Institute for Advanced Research, CIFAR Program in Gravity and the Extreme Universe, Toronto, ON, M5G 1Z8, Canada*
- <sup>54</sup>*Center for Astrophysics and Space Astronomy, Department of Astrophysical and Planetary Sciences, University of Colorado, Boulder, CO, 80309*
- <sup>55</sup>*Instituto de Física Teórica UAM/CSIC, Universidad Autónoma de Madrid, 28049 Madrid, Spain*
- <sup>56</sup>*European Southern Observatory, Karl-Schwarzschild-Straße 2, 85748 Garching, Germany*
- <sup>57</sup>*Department of Physics, University of Colorado, Boulder, CO, 80309*
- <sup>58</sup>*Santa Cruz Institute for Particle Physics, Santa Cruz, CA 95064, USA*
- <sup>59</sup>*University of Chicago, Chicago, IL 60637, USA*
- <sup>60</sup>*Harvard-Smithsonian Center for Astrophysics, Cambridge, MA 02138, USA*
- <sup>61</sup>*Australian Astronomical Observatory, North Ryde, NSW 2113, Australia*
- <sup>62</sup>*Departamento de Física Matemática, Instituto de Física, Universidade de São Paulo, CP 66318, São Paulo, SP, 05314-970, Brazil*
- <sup>63</sup>*Institut d'Astrophysique de Paris, F-75014, Paris, France*
- <sup>64</sup>*Steward Observatory, University of Arizona, 933 North Cherry Avenue, Tucson, AZ 85721*
- <sup>65</sup>*George P. and Cynthia Woods Mitchell Institute for Fundamental Physics and Astronomy, and Department of Physics and Astronomy, Texas A&M University, College Station, TX 77843, USA*
- <sup>66</sup>*Department of Astronomy, The Ohio State University, Columbus, OH 43210, USA*
- <sup>67</sup>*Department of Astrophysical Sciences, Princeton University, Peyton Hall, Princeton, NJ 08544, USA*
- <sup>68</sup>*Department of Physics, University of Chicago, Chicago, IL, USA 6063*
- <sup>69</sup>*Dunlap Institute for Astronomy & Astrophysics, University of Toronto, 50 St George St, Toronto, ON, M5S 3H4, Canada*
- <sup>70</sup>*Department of Physics, University of Minnesota, Minneapolis, MN, USA 55455*
- <sup>71</sup>*Department of Physics and Astronomy, Pevensey Building, University of Sussex, Brighton, BN1 9QH, UK*
- <sup>72</sup>*Physics Department, Center for Education and Research in Cosmology and Astrophysics, Case Western Reserve University, Cleveland, OH, USA 44106*
- <sup>73</sup>*Liberal Arts Department, School of the Art Institute of Chicago, Chicago, IL, USA 60603*
- <sup>74</sup>*School of Physics and Astronomy, University of Southampton, Southampton, SO17 1BJ, UK*
- <sup>75</sup>*Brandeis University, Physics Department, 415 South Street, Waltham MA 02453*
- <sup>76</sup>*Instituto de Física Gleb Wataghin, Universidade Estadual de Campinas, 13083-859, Campinas, SP, Brazil*
- <sup>77</sup>*Dept. of Physics, Stanford University, 382 Via Pueblo Mall, Stanford, CA 94305*
- <sup>78</sup>*Computer Science and Mathematics Division, Oak Ridge National Laboratory, Oak Ridge, TN 37831*
- <sup>79</sup>*Department of Astronomy & Astrophysics, University of Toronto, 50 St George St, Toronto, ON, M5S 3H4, Canada*
- <sup>80</sup>*Argonne National Laboratory, 9700 South Cass Avenue, Lemont, IL 60439, USA*
- <sup>81</sup>*Berkeley Center for Cosmological Physics, Department of Physics, University of California, and Lawrence Berkeley National Labs, Berkeley, CA, USA 94720*
- (Dated: October 8, 2018)

We cross-correlate galaxy weak lensing measurements from the Dark Energy Survey (DES) year-one (Y1) data with a cosmic microwave background (CMB) weak lensing map derived from South Pole Telescope (SPT) and *Planck* data, with an effective overlapping area of 1289 deg<sup>2</sup>. With the combined measurements from four source galaxy redshift bins, we reject the hypothesis of no lensing with a significance of 10.8 $\sigma$ . When employing angular scale cuts, this significance is reduced to 6.8 $\sigma$ , which remains the highest signal-to-noise measurement

of its kind to date. We fit the amplitude of the correlation functions while fixing the cosmological parameters to a fiducial  $\Lambda$ CDM model, finding  $A = 0.99 \pm 0.17$ . We additionally use the correlation function measurements to constrain shear calibration bias, obtaining constraints that are consistent with previous DES analyses. Finally, when performing a cosmological analysis under the  $\Lambda$ CDM model, we obtain the marginalized constraints of  $\Omega_m = 0.261^{+0.070}_{-0.051}$  and  $S_8 \equiv \sigma_8 \sqrt{\Omega_m/0.3} = 0.660^{+0.085}_{-0.100}$ . These measurements are used in a companion work that presents cosmological constraints from the joint analysis of two-point functions among galaxies, galaxy shears, and CMB lensing using DES, SPT and *Planck* data.

## I. INTRODUCTION

As a photon from a distant source travels through the Universe, its path is perturbed by the gravitational potential of large-scale structure, an effect known as gravitational lensing (for a review see e.g. [1]). The observed amplitude of the perturbations to the photon's trajectory depends on both the matter distribution and geometry of the Universe, making gravitational lensing a powerful cosmological probe. Furthermore, because these perturbations are induced by gravitational effects, they are sensitive to all forms of matter, including dark matter, which is difficult to probe by other means. The use of gravitational lensing to constrain cosmology has developed rapidly over the last decade [2–10] due to improvements in instrumentation and modeling, and increases in the cosmological volumes probed by surveys [11, 12].

In this study, we use two sources of photons to measure the effect of gravitational lensing: distant galaxies and the cosmic microwave background (CMB). Gravitational lensing caused by the large-scale distribution of matter distorts the apparent shapes of distant galaxies; similarly, gravitational lensing distorts the observed pattern of temperature fluctuations on the CMB last scattering surface. These distortions are expected to be correlated over the same patch of sky since the CMB photons pass through some of the same intervening gravitational potentials as the photons from distant galaxies. The two-point correlation between the galaxy lensing and CMB lensing fields can therefore be used as a cosmological probe.

Several features of the cross-correlation between galaxy lensing and CMB lensing make it an appealing cosmological observable. First, unlike two-point correlations between galaxies and lensing, the lensing-lensing correlation considered here has the advantage that it is not sensitive to difficult-to-model effects such as galaxy bias [13]. Second, since it is a cross-correlation between two independently measured lensing fields from datasets of completely different nature, it is expected to be relatively robust to observational systematics. For instance, systematics associated with galaxy shape measurement, like errors in the estimate of the point spread function, will have no impact on the inference of CMB lensing. Third, the use of the CMB lensing field provides sensitivity to the distance to the last scattering surface; the large distance to the last scattering surface in turn provides a long lever arm for constraining cosmology.

Measurement of the two-point correlation between galaxy lensing and CMB lensing was first reported by [14] using CMB lensing measurements from the Atacama Cosmology Telescope [15] and galaxy lensing measurements from the Canada-France-Hawaii Telescope Stripe-82 Survey [16]. Several subsequent measurements were made by [17] (*Planck*

CMB lensing + CFHTLenS galaxy lensing), [18] (*Planck* and SPT CMB lensing + DES-SV galaxy lensing), [19] (*Planck* CMB lensing + CHTLenS and RCSLenS galaxy lensing), and [20] (*Planck* CMB lensing + KiDS-450 galaxy lensing).

Here we measure the correlation between CMB lensing and galaxy lensing using CMB data from the South Pole Telescope (SPT) and *Planck*, and galaxy lensing data from year-one (Y1) observations of the Dark Energy Survey (DES; [21]). We perform a number of robustness checks on the measurements and covariance estimates to show that there is no evidence for significant systematic biases in the measurements over the range of angular scales that we include in the model fits.

The measurements presented here represent the highest signal-to-noise constraints on the cross-correlation between galaxy lensing and CMB lensing to date. We use the measured correlation functions to place constraints on cosmological parameters (in particular  $\Omega_m$  and  $S_8 = \sigma_8 \sqrt{\Omega_m/0.3}$ ). The cosmological constraints obtained here are complementary to those from DES-Y1 galaxy clustering and weak lensing [12], which are sensitive to somewhat lower redshifts.

This work is part of a series of four papers that use cross-correlations between DES data and CMB lensing measurements to constrain cosmology:

- Measurement of correlation between galaxy lensing and CMB lensing (this paper)
- Measurement of correlation between galaxies and CMB lensing [22]
- Methodology for analyzing joint measurements of correlations between DES data and CMB lensing [23]
- Results of joint analysis of correlations between DES data and CMB lensing [24].

The main goal of this work is to present the measurement of the correlation between galaxy lensing and CMB lensing, and to subject this measurement to robustness tests. Consequently, we keep discussion of the cosmological modeling brief and refer the readers to [23] for a more in depth discussion of the cosmological modeling used in these papers.

This work is organized as follows. In Sec. II we present the theoretical background of the analysis and the required formalism used throughout the analysis. We describe the data products used in Sec. III and the methodology used to make the measurements in Sec. IV. The results are presented in Sec. V, while the cosmological parameter fits are shown in Sec. VI. Finally, we present our conclusions in Sec. VII.

## II. THEORY

We are interested in the cross-correlation between CMB lensing and galaxy lensing. CMB lensing is typically measured in terms of the spin-0 lensing convergence,  $\kappa$ , which is proportional to a (weighted) integral along the line of sight of the matter density [25]. Galaxy lensing, on the other hand, is most easily measured via the spin-2 shear field,  $\gamma$ , by measuring shapes of many galaxies. The  $\gamma$  and  $\kappa$  signals are related, and one could in principle convert from  $\gamma$  to  $\kappa$  [e.g. 26]. However, the conversion process is lossy, and not necessary for our purposes since we can directly correlate  $\kappa$  and  $\gamma$ . The galaxy shear signal is estimated from the coherent distortion of the shapes of galaxies. In this analysis, we measure the correlation of the CMB lensing convergence,  $\kappa_{\text{CMB}}$ , with the *tangential* component of the galaxy shear,  $\gamma_t$  (i.e. the component orthogonal to the line connecting the two points being correlated). The advantages of using  $\gamma_t$  are that it is trivially computed from the observed shear and that  $\gamma_t$  is expected to be robust to additive systematics in the shear measurement process.<sup>1</sup> This approach was recently used by [19], who found it to yield higher signal-to-noise than alternative approaches; the same approach was also taken by [27].

To quantify the correlation between CMB lensing and galaxy lensing, we use the angular two-point function,  $w^{\gamma_t \kappa_{\text{CMB}}}(\theta)$ . To model this correlation, we begin by calculating the theoretical cross-power spectrum between the CMB lensing convergence and the galaxy lensing convergence,  $\kappa_{\text{CMB}}$  and  $\kappa_s$ , which we denote with  $C^{\kappa_s \kappa_{\text{CMB}}}(\ell)$ . In harmonic-space and using the Limber approximation [28, 29], we have:

$$C^{\kappa_s \kappa_{\text{CMB}}}(\ell) = \int_0^{\chi_*} \frac{d\chi}{\chi^2} q_{\kappa_s^i}(\chi) q_{\kappa_{\text{CMB}}}(\chi) P_{\text{NL}} \left( k = \frac{\ell + \frac{1}{2}}{\chi}, z(\chi) \right), \quad (1)$$

$$q_{\kappa_s^i} = \frac{3\Omega_m H_0^2}{2c^2} \frac{\chi}{a(\chi)} \int_{\chi}^{\chi_h} d\chi' \frac{n_s^i(z(\chi')) \frac{dz}{d\chi'}}{\bar{n}_s^i} \frac{\chi' - \chi}{\chi'}, \quad (2)$$

$$q_{\kappa_{\text{CMB}}}(\chi) = \frac{3\Omega_m H_0^2}{2c^2} \frac{\chi}{a(\chi)} \frac{\chi_* - \chi}{\chi_*}. \quad (3)$$

Here,  $\chi$  is the comoving distance,  $\chi_*$  is the comoving distance to the last scattering surface,  $a(\chi)$  is the cosmological scale factor at distance  $\chi$ ,  $n_s^i(z)$  is the redshift distribution of the source galaxies in the  $i$ th redshift bin,  $\bar{n}_s^i = \int dz n_s^i(z)$  is the angular number density in this redshift bin, and  $P_{\text{NL}}(k, z)$  is the non-linear matter power spectrum at wavenumber  $k$  and redshift  $z$ . We calculate  $P_{\text{NL}}$  using the Boltzmann code CAMB<sup>2</sup> [30, 31] with the Halofit extension to nonlinear scales [32, 33] and the [34] neutrino extension.

The harmonic-space cross-spectrum between the CMB and galaxy convergences can be transformed to a position-space

correlation function by taking the Hankel transform

$$w^{\gamma_t \kappa_{\text{CMB}}}(\theta) = \int_0^\infty \frac{\ell d\ell}{2\pi} C^{\kappa_s \kappa_{\text{CMB}}}(\ell) J_2(\ell\theta) F(\ell), \quad (4)$$

where  $J_2$  is the second order Bessel function of the first kind and  $F(\ell)$  describes filtering that is applied to the CMB lensing map (see §III). We set

$$F(\ell) = \begin{cases} \exp(-\ell(\ell+1)/\ell_{\text{beam}}^2), & \text{for } 30 < \ell < 3000 \\ 0, & \text{otherwise,} \end{cases} \quad (5)$$

with  $\ell_{\text{beam}} \equiv \sqrt{16 \ln 2} / \theta_{\text{FWHM}} \approx 2120$ , where  $\theta_{\text{FWHM}} = 5.4'$ . The low and high-pass  $\ell$  cuts are imposed to reduce biases in the CMB lensing map; the Gaussian smoothing is applied to ensure that large oscillations are not introduced when transforming from harmonic to position-space (i.e. aliasing from band limited measurements).

## III. DATA

### A. Galaxy weak lensing

DES is an optical galaxy survey conducted using the 570 Megapixel DECam instrument [35] mounted on the Blanco Telescope at the Cerro Tololo Inter-American Observatory (CTIO) located in Chile. In this analysis, we use the Y1 data that are based on observation runs between August 2013 and February 2014 [36]. We only use the data in the area overlapping with the SPT footprint<sup>3</sup>; the overlap area is approximately  $1289 \text{ deg}^2$  between  $-60^\circ < \text{Dec.} < -40^\circ$ , after applying a mask to remove poorly characterized regions.

Two independent shape measurement algorithms — METACALIBRATION and IM3SHAPE — were used to generate two different shear catalogs from DES-Y1 data. These algorithms and the corresponding catalogs are described in detail in [37]. In this analysis, we only consider the METACALIBRATION shear estimates because of the higher signal-to-noise ratio of that catalog.

METACALIBRATION [38, 39] is a recently developed technique for measuring galaxy shears that uses the data itself for calibration, rather than relying on external image simulations. The methodology has been demonstrated to yield a multiplicative shear bias below  $10^{-3}$  on simulations with galaxies of realistic complexity [39]. Briefly, METACALIBRATION performs shear calibration by applying artificial shears to the observed galaxy images and measuring the response of the shear estimator. The shear catalog used in this work was based on jointly fitting images in three bands (*riz*).

The full METACALIBRATION catalogue is split into 4 photometric redshift bins:  $0.20 < z < 0.43$ ,  $0.43 < z < 0.63$ ,  $0.63 < z < 0.90$ ,  $0.90 < z < 1.30$ , where  $z$  is the mean of the estimated redshift probability distribution for each galaxy and

<sup>1</sup> Any additive systematic affecting the shear measurements that is constant over scales of interest will vanish when averaging  $\gamma_t$  over azimuthal angle; this is not true for the Cartesian components of  $\gamma$ .

<sup>2</sup> See `camb.info`.

<sup>3</sup> DES-Y1 data also covers the SDSS Stripe-82 region, though the cosmology analysis focuses on the SPT region.

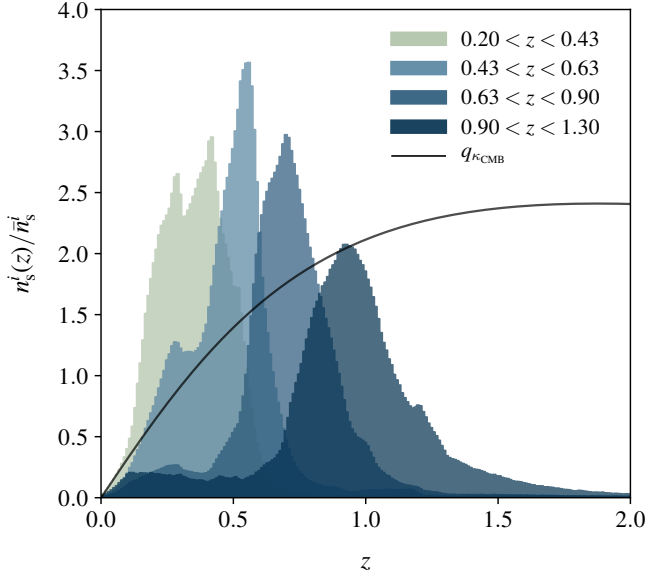


FIG. 1. Redshift distribution of galaxies  $n_s^i(z)$  for the 4 tomographic bins for METACALIBRATION. The black line shows the CMB lensing kernel.

the binning is chosen to be consistent with that used in [12]. The redshift distributions,  $n_s^i(z)$ , for each of the samples were estimated using the BPZ code [40]. Detailed validation of these distributions can be found in [41–43]. We also checked that using an independent  $n_s^i(z)$  estimation from the high quality COSMOS2015 photometric redshift catalog [41, 44] results in negligible change in the final cosmological constraints.

To avoid implicit experimenter bias, the measurements were blinded while most of the analysis was being performed. The measurements were not compared with theoretical predictions and the axes were removed prior to unblinding. For cosmological parameters estimations, the contours were shifted, and the axes were removed.

## B. CMB lensing map

We use the CMB weak lensing map described in [45], which was created from a combination of the SPT and *Planck* CMB temperature data. Details of the  $\kappa_{\text{CMB}}$  procedures used to create the map can be found in [45]; we provide a brief overview below.

The lensing map is derived from a minimum-variance combination of SPT 150 GHz and *Planck* 143 GHz temperature maps over the SPT-SZ survey region ( $20^{\text{h}}$  to  $7^{\text{h}}$  in right ascension and from  $-65^\circ$  to  $-40^\circ$  in declination). By combining SPT and *Planck* maps in this way, the resultant temperature map is sensitive to a greater range of modes on the sky than either experiment alone. Modes in the temperature maps with  $\ell > 3000$  are removed to avoid systematic biases due to astrophysical foregrounds such as the thermal Sunyaev-Zel’dovich effect (tSZ) and the cosmic infrared background (CIB) [46],

whereas modes with  $\ell < 100$  are removed to reduce the effects from low-frequency noise. The quadratic estimator technique [47] is used to construct a (filtered) estimate of  $\kappa_{\text{CMB}}$ . Simulations are used to remove the mean-field bias and to calculate the response function which is used to properly normalize the amplitude of the filtered lensing map.

The output lensing convergence map is filtered further to remove modes with  $\ell < 30$  and  $\ell > 3000$  and is smoothed with a Gaussian beam with full width at half maximum of  $5.4'$ . Point sources (dusty-star forming and radio galaxies) with flux density above 6.4 mJy in the 150 GHz band are masked with apertures of  $r = 3', 6', 9'$  depending the brightness of the point source. Additionally, in order to reduce contamination of the  $\kappa_{\text{CMB}}$  map by thermal Sunyaev-Zel’dovich (tSZ) signal, we apply a mask to remove clusters detected at signal-to-noise  $S/N > 5$  in the SPT CMB maps, and DES REDMAPPER clusters with richness  $\lambda > 80$ ; these clusters are masked with an aperture of  $r = 5'$ . The effectiveness of this masking at reducing tSZ contamination was investigated in [23]. Such masking could in principle induce a bias because clusters are associated with regions of high lensing convergence. However, it was shown in [23] that this bias is negligible due to the small fraction of area masked relative to the total area used.<sup>4</sup>

The effect of the uncertainty on the calibration of the CMB temperature was investigated in [45], and it was found to be at most  $0.20\sigma$  of the statistical uncertainty when the calibration is conservatively varied by 1% (although it is known to better than 1% as noted in [48]).

## IV. METHODS

### A. Two-point measurement

Our estimator for the angular correlation function at the angular bin specified by angle  $\theta_\alpha$  is

$$w^{\gamma_{\text{CMB}}}(\theta_\alpha) = \frac{\sum_{i=1}^{N_{\text{pix}}} \sum_{j=1}^{N_{\text{gal}}} f_\kappa^i \kappa_{\text{CMB}}^i e_t^{ij} \Theta_\alpha(\hat{\theta}^i - \hat{\theta}^j)}{s(\theta_\alpha) \sum f_\kappa^i}, \quad (6)$$

where the sum in  $i$  is over all pixels in the CMB convergence map, the sum in  $j$  is over all source galaxies, and  $\hat{\theta}$  represents the direction of the  $\kappa_{\text{CMB}}$  pixels or source galaxies.  $e_t^{ij}$  is the component of the corrected ellipticity oriented orthogonally to the line connecting pixel  $i$  and source galaxy  $j$  [see e.g. 49]. The  $\kappa_{\text{CMB}}$  value in the pixel is  $\kappa_{\text{CMB}}^i$  and  $f_\kappa^i$  is the associated pixel masking weight, which takes a value between zero and one (i.e. zero if the pixel is completely masked). The function  $\Theta_\alpha(\theta)$  is an indicator function that is equal to unity when the angular separation between  $\hat{\theta}_i$  and  $\hat{\theta}_j$  is in the angular bin specified by  $\theta_\alpha$ , and zero otherwise. Finally,  $s(\theta_\alpha)$  is the METACALIBRATION response, which can be estimated from the data using the procedure described in [37]. We find that  $s(\theta)$  is

<sup>4</sup> Less than 1% of the survey area is lost by applying a mask that removes 437 clusters.



approximately constant over the angular scales of our interest, but different for each redshift bin. We evaluate the estimator in Eq. 6 using the TREECORR package.<sup>5</sup>

We perform the  $w^{\gamma_i \kappa_{\text{CMB}}}(\theta)$  measurements in 10 logarithmic bins over the angular range  $2.5' < \theta < 250'$ . Later we remove a sub-range of these scales in the likelihood analysis, where the scale cuts are determined such that they prevent known sources of systematic error from biasing cosmological constraints (see Sec. IV D).

## B. Modelling of systematic effects in galaxy shear measurements

Eq. 4 forms the basis for our model of the measured correlation functions. We improve on this basic model by also incorporating prescriptions for systematic errors in the estimated shears and redshift distributions of the galaxies. We describe these models briefly below. For more details, readers should refer to [23] and [50]. The computation of the model vectors and sampling of parameter space is performed using COSMOSIS [30, 32, 51–56].

### 1. Photometric redshift bias

The inference of the redshift distribution,  $n_s^i(z)$ , for the source galaxy sample is potentially subject to systematic errors. Following [23], [50] and related past work [5, 57–59], we account for these potential systematic errors in the modeling by introducing a photometric redshift bias parameter which shifts the assumed  $n_s^i(z)$  for the source galaxies. That is, the true redshift distribution for the  $i$ th source galaxy bin,  $n_{s,\text{unbiased}}^i(z)$ , is related to the observed redshift distribution,  $n_s^i(z)$ , via:

$$n_{s,\text{unbiased}}^i(z) = n_s^i(z - \Delta_{z,s}^i), \quad (7)$$

where  $\Delta_{z,s}^i$  is the redshift bias parameter, which is varied independently for each source galaxy redshift bin.

Priors on the  $\Delta_{z,s}^i$  are listed in Table I. The  $\Delta_{z,s}^i$  values for the three lowest redshift bins were obtained by cross-correlating the source galaxy sample with REDMAGIC Luminous Red Galaxies (LRGs) [60], which have well characterized redshifts. The  $\Delta_{z,s}^i$  value for the highest redshift bin comes from comparing  $n_s^i(z)$  derived from BPZ and the COSMOS2015 catalog. The derivation of these priors is described in [41], with two other supporting analyses described in [42] and [43].

### 2. Shear calibration bias

In weak lensing, one estimates galaxy shapes, or ellipticities using a suitably chosen estimator. These estimators are often biased and need to be *calibrated* using either external image

simulations (e.g. the IM3SHAPE method) or manipulation of the data itself (e.g. the METACALIBRATION method). The shear calibration bias refers to the residual bias in the shear estimate after the calibration process, or the uncertainty in the calibration process. In particular, we are mainly concerned about the multiplicative bias in the shear estimate, which can arise from failures in the shape measurements, stellar contamination in the galaxy sample, false object detection and selection bias [61, 62].

Following [23] and [50], we parameterize this systematic error in shear calibration with a single multiplicative factor,  $(1 + m_i)$ , for each redshift bin  $i$ . With this factor, the observed correlation function becomes:

$$w_{\text{obs}}^{\gamma_i \kappa_{\text{CMB}}}(\theta) = (1 + m_i) w_{\text{true}}^{\gamma_i \kappa_{\text{CMB}}}(\theta) \quad i \in \{1, 2, 3, 4\}. \quad (8)$$

We let the bias parameter for each redshift bin vary with a Gaussian prior listed in Table I based on [37].

### 3. Intrinsic alignment

In addition to the apparent alignment of the shapes of galaxies as a result of gravitational lensing, galaxy shapes can also be *intrinsically* aligned as a result of their interactions with the tidal field from nearby large scale structure. The intrinsic alignment (IA) effect will impact the observed correlation functions between galaxy shear and  $\kappa_{\text{CMB}}$  [63, 64]. The impact of IA can be modeled via:

$$C_{\text{obs}}^{\kappa_s \kappa_{\text{CMB}}}(\ell) = C_{\text{true}}^{\kappa_s \kappa_{\text{CMB}}}(\ell) - C^{\kappa_{\text{CMB}} \text{I}}(\ell), \quad (9)$$

where  $C^{\kappa_{\text{CMB}} \text{I}}(\ell)$  is calculated in a similar way as Eq. 1, but with replacing the galaxy lensing kernel with:

$$W^{\text{I}}(\chi) = A(\chi(z)) \frac{C_1 \rho_{\text{crit}} \Omega_m}{\mathcal{D}(z)} \frac{n_s^i(z(\chi))}{\bar{n}_s} \frac{dz}{d\chi}, \quad (10)$$

where  $\mathcal{D}(z)$  is the linear growth function. Here we have employed the non-linear linear alignment model (see [52] for details) and included the redshift evolution of the IA amplitude via

$$A(\chi(z)) = A^{\text{IA}} \left( \frac{1+z}{1+z_0} \right)^{\eta^{\text{IA}}}, \quad (11)$$

We use fixed values  $z_0 = 0.62$ ,  $C_1 \rho_{\text{crit}} = 0.0134$ , while letting  $A^{\text{IA}}$  and  $\eta^{\text{IA}}$  vary, as done in [12].

## C. Covariance

The covariance matrix of  $w^{\gamma_i \kappa_{\text{CMB}}}(\theta)$  is computed analytically, using the halo-model to estimate the non-Gaussian contributions. Details of the covariance calculation can also be found in [23] and [50]. However, we make a small modification in calculating the noise-noise covariance term, which we measure by cross-correlating  $\kappa_{\text{CMB}}$  noise and rotated galaxy shears. This modification is needed to incorporate the geometry of the mask, which the analytic covariance neglects, and

<sup>5</sup> <https://github.com/rmjjarvis/TreeCorr>

PARAMETER	FIDUCIAL	PRIOR
COSMOLOGY		
$\Omega_m$	0.309	[0.1, 0.9]
$A_s/10^{-9}$	2.14	[0.5, 5.0]
$n_s$	0.967	[0.87, 1.07]
$w_0$	-1.0	FIXED
$\Omega_b$	0.0486	[0.03, 0.07]
$h_0$	0.677	[0.55, 0.91]
$\Omega_\nu h^2$	$6.45 \times 10^{-4}$	[0.0006, 0.01]
$\Omega_K$	0	FIXED
$\tau$	0.066	FIXED
SHEAR CALIBRATION BIAS		
$m^1$	0.010	(0.012, 0.023)
$m^2$	0.014	(0.012, 0.023)
$m^3$	0.006	(0.012, 0.023)
$m^4$	0.013	(0.012, 0.023)
INTRINSIC ALIGNMENT		
$A^{IA}$	0.44	[-5, 5]
$\eta^{IA}$	-0.67	[-5, 5]
$z_0$	0.62	FIXED
SOURCE PHOTO-Z ERROR		
$\Delta_{z,s}^1$	-0.004	(-0.001, 0.016)
$\Delta_{z,s}^2$	-0.029	(-0.019, 0.013)
$\Delta_{z,s}^3$	0.006	(0.009, 0.011)
$\Delta_{z,s}^4$	-0.024	(-0.018, 0.022)

TABLE I. The fiducial parameter values<sup>a</sup> and priors for cosmological and nuisance parameters used in this analysis. Square brackets denote a flat prior over the indicated range, while parentheses denote a Gaussian prior of the form  $\mathcal{N}(\mu, \sigma)$ .

<sup>a</sup> We use the *Planck* TT,TE,EE+LENSING+EXT best-fit values from [65] for the cosmological parameters and the marginalized 1D peaks for the DES nuisance parameters from the DES-Y1 joint analysis [12].

this correction increases the covariance by  $\sim 30\%$ . We compare the theoretical estimate of the covariance to an estimate of the covariance derived from the data in Sec. VB.

### D. Angular scale cuts

There are several effects that may impact the observed correlation functions that we do not attempt to model. As shown in [23], the most significant unmodelled effects for the analysis of  $w^{\gamma_t \kappa_{\text{CMB}}}$  are bias in  $\kappa_{\text{CMB}}$  due to the thermal Sunyaev-Zel'dovich (tSZ) effect, and the impact of baryonic effects on the matter power spectrum. To prevent these effects from introducing systematic errors into our cosmological constraints, we exclude the angular scales from our analysis that are most impacted. The tSZ bias is greatest at approximately 3–5 Mpc and slowly decreases at both smaller and larger scales. In contrast, the impact of the baryonic effects is greatest below roughly 4 Mpc, and negligible at larger scales (see Fig. 4 of [23]). Based on these results, it was demonstrated that the impact of the sum of these effects can be mitigated by excluding small scales from the analysis.

In this study we adopt the scale cuts directly from [23]. The scale cuts exclude angular bins below 40 arcminutes for the two lowest redshift bins, and scales below 60 arcminutes for the

two highest redshift bins.<sup>6</sup> For the angular scales beyond the scale cuts, the baryonic effects have negligible impact to our measurements, while the tSZ effect still remains. We quantify this residual bias in Sec. VC.

We note that the scale cut choices made in this analysis were motivated from consideration of the full  $5 \times 2$ pt data vector, and not from consideration of  $w^{\gamma_t \kappa_{\text{CMB}}}(\theta)$  alone. This choice was made because one of the main purposes of this work is to provide the measurements of  $w^{\gamma_t \kappa_{\text{CMB}}}(\theta)$  that will be incorporated into the companion analysis of [24]. Since the other four two-point functions also contribute some potential bias in the  $5 \times 2$ pt analysis, the scale cut choice adopted here is conservative for the analysis of  $w^{\gamma_t \kappa_{\text{CMB}}}(\theta)$  alone.

## V. MEASUREMENT

The measured two-point angular correlation functions,  $w^{\gamma_t \kappa_{\text{CMB}}}(\theta)$ , for each of the source galaxy bins are shown in Fig. 2. For each redshift bin we measure the correlation function in 10 angular bins logarithmically spaced between 2.5 and 250 arcminutes. We choose this binning to preserve reasonable signal-to-noise in each angular bin, as discussed in [23].

### A. Testing the measurements

#### 1. Correlation of $\kappa_{\text{CMB}}$ with $\gamma_\times$

When cross-correlating the observed galaxy shears with the  $\kappa_{\text{CMB}}$  map, we divide the observed shear into a tangential component,  $\gamma_t$ , oriented tangentially to the line connecting the two points being correlated, and a cross component,  $\gamma_\times$ , which is parallel to the line connecting the two points. Weak lensing is expected to produce a tangential shear component only, and therefore the presence of a non-zero cross-correlation with the cross-shear component would indicate the presence of systematic errors.

In Fig. 2, we show the measured cross-correlation between the  $\kappa_{\text{CMB}}$  maps and the cross-component of the shear (open points). As expected, we find that the measured cross-correlation is consistent with zero in all redshift bins. We calculate the  $\chi^2/\nu$  (where  $\nu$  is the number of degrees of freedom) and probability-to-exceed (p.t.e.) between the measurement and the null hypothesis (zero cross-correlation) for all redshift bins combined, applying the angular scale cuts described in Sec. IV D, and find  $\chi^2/\nu = 6.9/14$  and p.t.e = 0.94, indicating consistency of the cross-shear correlation with zero. The  $\chi^2/\nu$  and p.t.e for the individual bins are summarized in Table II.

<sup>6</sup> These angular scales cuts are applied to the two-point correlation measurement between galaxy weak lensing and the CMB lensing map, not the temperature map that is used to reconstruct the lensing map.

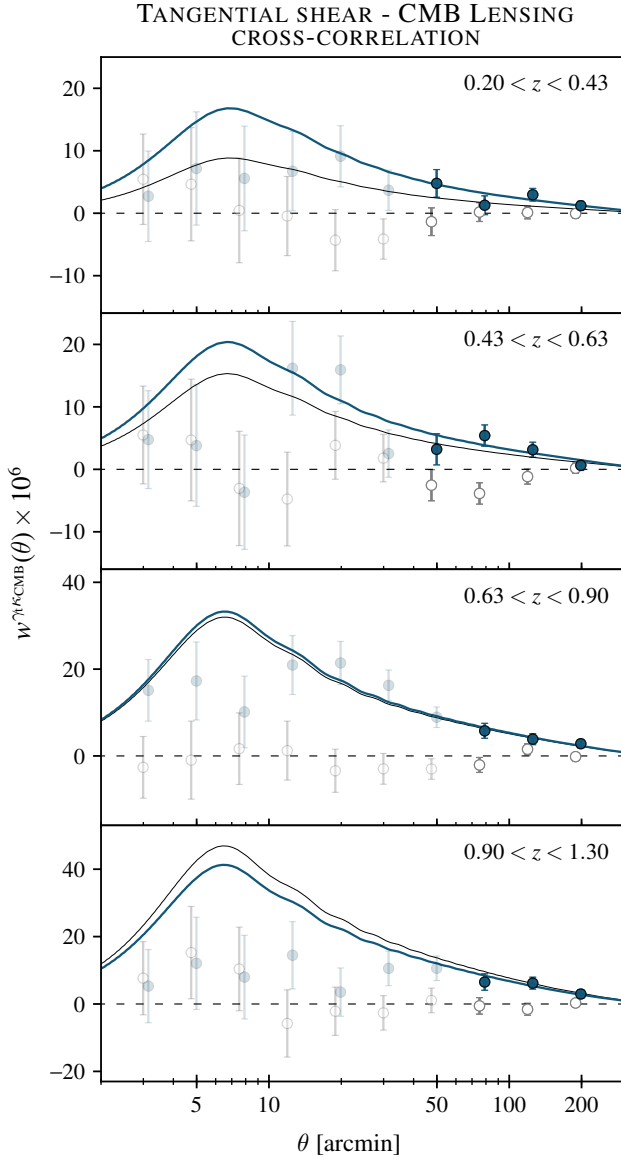


FIG. 2. Measurements of  $w^{\gamma_{\text{KCMB}}}(\theta)$  (filled circles) and  $w^{\gamma_{\text{KCMB}}}(\theta)$  (open circles) using METACALIBRATION shear estimates and the SPT+Planck CMB lensing map. The four panels show results for the four source galaxy redshift bin. Faded points are removed from the final analysis due to systematics or uncertainties in the modeling. Also shown are the theoretical predictions using fiducial cosmology with  $A = 1$  (black), and with best-fit  $A$  (blue), where  $A$  is defined in Sec. VIA.

### B. Testing the covariance

As mentioned in Sec. IV B, we employ a theoretical covariance matrix (with a small empirical modification) when fitting the measured correlation functions. To test whether the theoretical covariance accurately describes the noise in the measurements, we compare it to an estimate of the covariance obtained using the “delete-one” jackknife method applied to data.

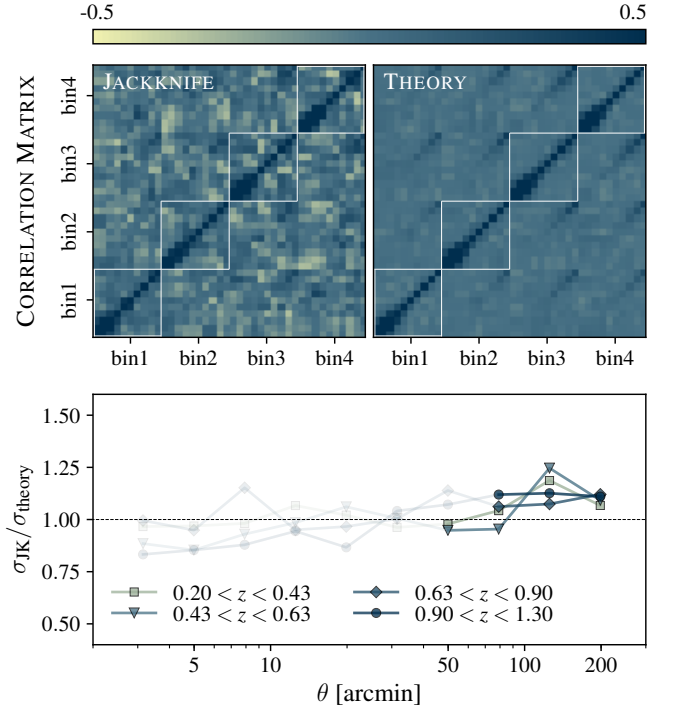


FIG. 3. The jackknife (upper left) and theory (upper right) correlation matrix ( $C_{ij}/\sqrt{C_{ii}C_{jj}}$ ) for all the redshift bins. Lower panel: ratio of the diagonal component of the covariance matrix for the theory and the jackknife covariance in all redshift bins showing an agreement to within 25% (shown as the gray band) for all the redshift bins.

To compute the jackknife covariance estimate, we divide the source galaxy samples into  $N_{\text{jk}} = 100$  approximately equal-area patches. The jackknife estimate of the covariance is then computed as

$$\mathbf{C}_{ij}^{\text{jackknife}} = \frac{N_{\text{jk}} - 1}{N_{\text{jk}}} \sum_k (d_i^k - \bar{d}_i)(d_j^k - \bar{d}_j), \quad (12)$$

where  $d_i^k$  is  $i$ th element of the  $w^{\gamma_{\text{KCMB}}}(\theta)$  data vector that is measured after excluding the shears in the  $i$ th patch on the sky, and  $\bar{d}$  is

$$\bar{d}_i = \frac{1}{N_{\text{jk}}} \sum_k d_i^k. \quad (13)$$

We have validated the jackknife approach to estimating the covariance matrix of  $w^{\gamma_{\text{KCMB}}}(\theta)$  using simulated catalogs. The validation tests are described in Appendix B.

The theoretical and jackknife estimates of the covariance matrix, and the ratio between the diagonal elements of the two are shown in Fig. 3. It is clear from the top panels of the figure that the covariance structure of the theoretical covariance agrees qualitatively with the covariance measured from the data. Furthermore, the bottom panel shows that the two covariances agree along the diagonal to better than 25%<sup>7</sup> across

<sup>7</sup> 25% is approximately the scatter we see when comparing the covariance



all redshift bins.

### C. Estimating the impact of unmodeled systematics

While some sources of systematic error are modeled in the analysis (namely photometric redshift and multiplicative shear biases), there are several other potential sources of systematic errors coming from unmodeled effects that could impact the measurement of  $w^{\gamma_t \kappa_{\text{CMB}}}(\theta)$ . Some of these, such as tSZ bias, are minimized with angular scale cuts. One useful diagnostic to determine the impact of residual systematic biases is to identify the list of external quantities that could directly or indirectly contaminate the signal and cross-correlate them with the measured galaxy shears and CMB convergence. We expect these cross-correlations to be consistent with zero if these external quantities are not introducing significant biases in the measurements. One example of a quantity that could correlate both with observed shear and CMB convergence is dust extinction: dust extinction is lower at high galactic latitudes, which is where the density of stars is lowest, and therefore, could result in poor PSF modelling and biased shear estimates in those areas. Meanwhile, dust is one of the foreground component of the CMB temperature measurements, and one can expect potential residuals in a single frequency temperature map. When a contaminated temperature map is passed through the lensing reconstruction pipeline, fluctuations from these foregrounds get picked up as false lensing signal, which will be spatially correlated with the variations in the galaxy shape measurements, and therefore introduce biases in our measurements.

We divide potential systematic contaminants into two categories: those that are expected to be correlated with the true (i.e. uncontaminated)  $\gamma$  or  $\kappa_{\text{CMB}}$ , and those that are not. For those systematics that are expected to be uncorrelated with the true  $\gamma$  and  $\kappa_{\text{CMB}}$ , we estimate the contamination of  $w^{\gamma_t \kappa_{\text{CMB}}}(\theta)$  via

$$w_S(\theta) = \frac{w^{\kappa_{\text{CMB}} S}(\theta) w^{\gamma_t S}(\theta)}{w^{SS}(\theta)}, \quad (14)$$

where  $S$  is the foreground map of interest. This expression captures correlation of the systematic with both  $\kappa_{\text{CMB}}$  and  $\gamma$ , and is normalized to have the same units as  $w^{\gamma_t \kappa_{\text{CMB}}}(\theta)$ . Unless the systematic map is correlated with both  $\gamma_t$  and  $\kappa_{\text{CMB}}$ , it will not bias  $w^{\gamma_t \kappa_{\text{CMB}}}(\theta)$  and  $w_S(\theta)$  will be consistent with zero.

We consider three potential sources of systematic error that are expected to be uncorrelated with the true  $\gamma$  and  $\kappa_{\text{CMB}}$ :  $\gamma_t^{\text{PSFres}}$  (the residual PSF ellipticity),  $E_{B-V}$  (dust extinction) and  $\delta_{\text{star}}$  (stellar number density). We use the difference between the PSF ellipticity between the truth (as measured from stars) and the model for the PSF residual. Descriptions of the  $E_{B-V}$  and  $\delta_{\text{star}}$  maps can be found in [66]. The measured  $w_S(\theta)$  for these quantities are plotted in Fig. 4 relative to the

uncertainties on  $w^{\gamma_t \kappa_{\text{CMB}}}(\theta)$ . The error bars shown are determined by cross-correlating the systematic maps with simulated  $\kappa_{\text{CMB}}$ ,  $\gamma_t$  maps generated using the FLASK package [67]. For each of the potential systematics considered, we find that the measured  $w_S(\theta)$  is much less than the statistical uncertainties on the  $w^{\gamma_t \kappa_{\text{CMB}}}(\theta)$  correlation, implying that there is very little impact from these systematics.

Astrophysical systematic effects that we expect to correlate with the true  $\gamma$  and  $\kappa_{\text{CMB}}$  must be treated somewhat differently, since in this case, Eq. 14 will not yield the expected bias in  $w^{\gamma_t \kappa_{\text{CMB}}}(\theta)$ . Two sources of potential systematic error are expected to have this property, namely contamination of the  $\kappa_{\text{CMB}}$  map by tSZ and the cosmic infrared background (CIB). Since the tSZ and CIB are both correlated with the matter density, these contaminants will be correlated with the true shear and  $\kappa_{\text{CMB}}$  signals. For both contaminants, we construct convergence maps of the contaminating fields across the DES patch, which we refer to as  $\kappa_{\text{tSZ}}$  and  $\kappa_{\text{CIB}}$ . The estimates of  $\kappa_{\text{tSZ}}$  and  $\kappa_{\text{CIB}}$  are generated as described in [23].

We estimate the bias induced to  $w^{\gamma_t \kappa_{\text{CMB}}}(\theta)$  by tSZ and CIB by measuring  $w^{\gamma_t \kappa_{\text{tSZ}}}(\theta)$  and  $w^{\gamma_t \kappa_{\text{CIB}}}(\theta)$ . These quantities are plotted in Fig. 4, with error bars determined by measuring the variance between the systematic maps with 100 simulated sky realizations generated using the FLASK simulations (see Appendix A for details). We measure a bias over the angular ranges of interest, with a maximum bias<sup>8</sup> of  $\sim 0.30\sigma$  (where  $\sigma$  is the expected standard deviation for  $w^{\gamma_t \kappa_{\text{CMB}}}(\theta)$ ). As shown in [23], this level of bias results in a small shift to inferred parameter constraints.

## VI. PARAMETER CONSTRAINTS

We assume a Gaussian likelihood for the data vector of measured correlation functions,  $\vec{d}$ , given a model,  $\vec{m}$ , generated using the set of parameters  $\vec{p}$ :

$$\ln \mathcal{L}(\vec{d}|\vec{m}(\vec{p})) = -\frac{1}{2} \sum_{ij}^N (d_i - m_i(\vec{p})) \mathbf{C}_{ij}^{-1} (d_j - m_j(\vec{p})), \quad (15)$$

where the sums run over all of the  $N$  elements in the data and model vectors. The posterior on the model parameters can be calculated as:

$$P(\vec{m}(\vec{p})|\vec{d}) \propto \mathcal{L}(\vec{d}|\vec{m}(\vec{p})) P_{\text{prior}}(\vec{p}), \quad (16)$$

where  $P_{\text{prior}}(\vec{p})$  is the prior on the model parameters.

In the following sections, we will use this framework to generate parameter constraints in four scenarios, each keeping different sets of parameters free.

computed from many FLASK (described in Appendix A.) realizations and using the jackknife method on a single FLASK realization.

<sup>8</sup> [23] uses theory data vectors and model fits to the measured biases to calculate similar quantities, from which the scale-cuts are derived. In contrast, the measurements shown in Fig. 4 are calculated using the  $\kappa_{\text{tSZ}}$  map and the galaxy shape catalogs, and therefore includes scatter. Although it may appear as though the scale cuts are removing less biased angular bins, this is primarily due to the scatter in our measurements.

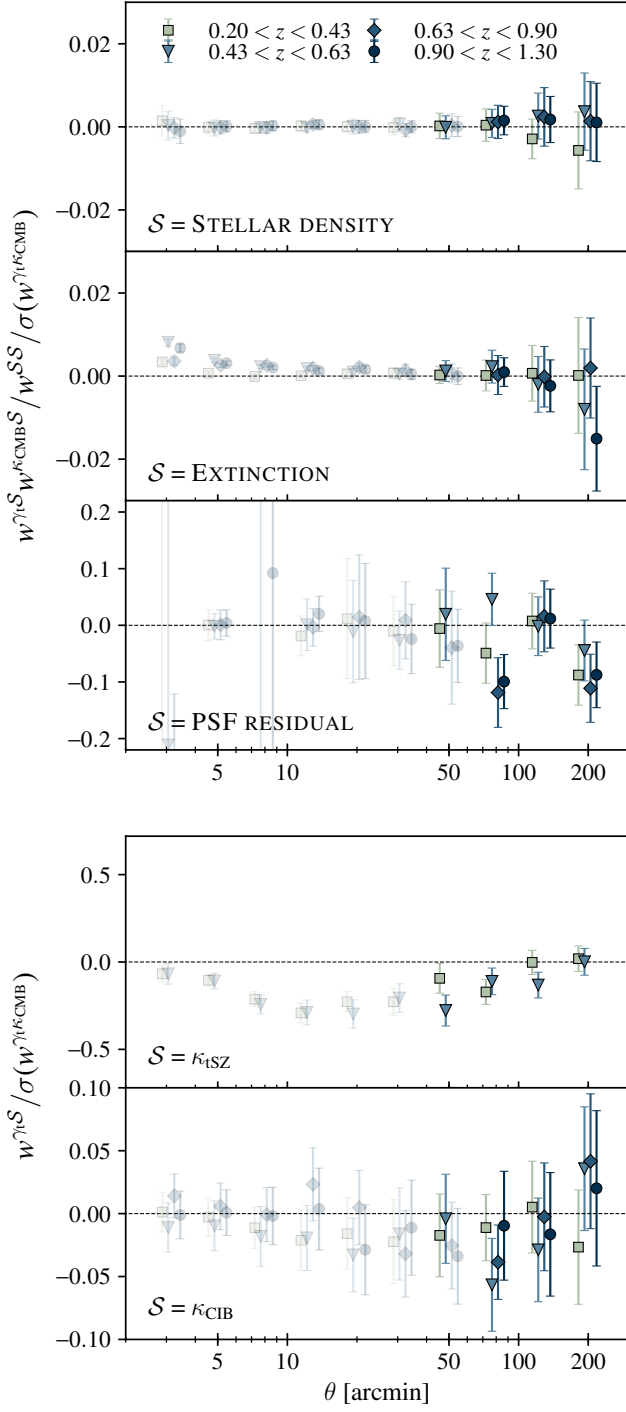


FIG. 4. Ratios of the estimated systematic biases to  $\gamma_t \kappa_{\text{CMB}}$  from various contaminants to the statistical uncertainties on  $\gamma_t \kappa_{\text{CMB}}$ . We find that all systematics considered result in negligible bias to the  $\gamma_t \kappa_{\text{CMB}}$  measurements. For the case of PSF residuals, the auto-correlation  $w^{SS}(\theta)$  of some bins are close to zero, resulting in large error bars for certain bins. As described in the text, contamination from the tSZ effect and the CIB (bottom two panels) must be treated somewhat differently from the other contaminants, since these two potential sources of bias are known to be correlated with the signal. While we find significant evidence for non-zero  $w^{\gamma_t \kappa_{\text{tSZ}}}(\theta)$ , the size of this correlation is small compared to the errorbars on  $w^{\gamma_t \kappa_{\text{CMB}}}(\theta)$ , and does not lead to significant biases in cosmological constraints.

We note that we made minor modifications to the analysis after we unblinded the data. We originally computed the constraints on shear calibration and intrinsic alignment parameters fixing the cosmology to the values obtained from DES-Y1 in Sec. VI B and VI C. We later allowed the cosmological parameters to vary but combined with the *Planck* baseline likelihood. Consequently, we also switched to using models generated assuming *Planck* best-fit values when fitting the correlation amplitudes in Sec. VI A, so that the same framework is used throughout the analysis.

### A. Amplitude fits

We first attempt to constrain the amplitude of the observed correlation functions relative to the expectation for the fiducial cosmological model summarized in Table I. The fiducial cosmological parameters are chosen to be the best-fitting parameters from the analysis of CMB and external datasets in [65]; and nuisance parameter values (shear calibration bias, intrinsic alignment and source redshift bias) are chosen to be the best-fitting parameters from the analysis of [12]. In this case, the model is given by  $\vec{d} = A \vec{d}_{\text{fid}}$ , where  $A$  is an amplitude parameter and  $\vec{d}_{\text{fid}}$  is the model for the correlation functions computed using the fiducial cosmological model of Table I. The model is computed as described in Sec. IV B.

The resultant constraints on  $A$  for each redshift bin (and for the total data vector) are summarized in Table II. We find that the measured amplitudes are consistent with  $A = 1$ , although the first redshift bin is marginally high. We calculate the p.t.e using the  $\chi^2$  of the measurement fit to the fiducial model with  $A = 1$  and obtain 0.14, which suggests that this deviation is not significant. We additionally note the mild correlation between  $A$  and redshift, although with our uncertainties, no conclusions could be made.

The constraint on  $A$  using all redshift bins is  $A = 0.99 \pm 0.17$ . Furthermore, the resultant  $\chi^2$  and p.t.e. values indicate that the model is a good description of the data. These values are shown in the rightmost columns of Table II. This measurement rejects the hypothesis of no lensing at a significance of  $6.8\sigma$ , and has a signal-to-noise ratio<sup>9</sup> of  $5.8\sigma$ . The latter value can be compared directly with results from past work: the cross-correlation measurement between Canada-France-Hawaii telescope stripe-82 survey and Atacama Cosmology Telescope obtained  $4.2\sigma$  [14], RCSLen and *Planck* obtained  $4.2\sigma$  [19], DES-SV and SPT-SZ obtained  $2.9\sigma$  [18], KiDS-450 and *Planck* obtained  $4.6\sigma$  [20]. We also estimate the detection significance and signal-to-noise ratio we would have obtained with no scale cuts and find  $10.8$  and  $8.2\sigma$ , respectively. (We note that biases due to tSZ and baryonic effects both tend to lower the cross-correlation amplitude; hence, these values are underestimates of the detection significance we would have found in the absence of these biases.)

<sup>9</sup> The two values are calculated using  $\sqrt{\chi^2_{\text{null}}}$  and  $\sqrt{\chi^2_{\text{null}} - \chi^2_{\text{min}}}$  respectively.

SAMPLE	A	$\chi^2/\nu$	p.t.e.
$0.20 < z < 0.43$	$1.90 \pm 0.53$	2.6/3 (0.4/4)	0.46 (0.98)
$0.43 < z < 0.63$	$1.33 \pm 0.36$	2.9/3 (8.9/4)	0.41 (0.06)
$0.63 < z < 0.90$	$1.04 \pm 0.22$	0.7/2 (4.3/3)	0.69 (0.23)
$0.90 < z < 1.30$	$0.88 \pm 0.20$	1.0/2 (0.7/3)	0.60 (0.87)
all bins	$0.99 \pm 0.17$	12.2/13 (6.9/14)	0.51 (0.94)

TABLE II. Results of the amplitude fitting analysis described in Sec. VI A, assuming *Planck* best-fit  $\Lambda$ CDM cosmology. Results shown correspond to METACALIBRATION measurements with angular scale cuts applied. The numbers in enclosed in parentheses are fits for  $\gamma_\times$  to  $A = 0$ .

SAMPLE	$\gamma_{t\kappa\text{CMB}}$	$\gamma\gamma$
$0.20 < z < 0.43$	--	$0.02^{+0.15}_{-0.16}$
$0.43 < z < 0.63$	$-0.08^{+0.47}_{-0.31}$	$-0.04^{+0.09}_{-0.10}$
$0.63 < z < 0.90$	$-0.06^{+0.20}_{-0.28}$	$-0.10^{+0.05}_{-0.05}$
$0.90 < z < 1.30$	$-0.14^{+0.14}_{-0.28}$	$-0.05^{+0.06}_{-0.06}$

TABLE III. Constraints on  $m^i$  from combining  $\gamma_{t\kappa\text{CMB}}$  and  $\gamma\gamma$  with the *Planck* baseline likelihood. The constraints we obtain here are weaker than those obtained through other simulation and data based calibration methods described in [37].

### B. Constraining shear calibration bias

In this section and Sec. VI C, we marginalize over the cosmological parameters and nuisance parameters (shear calibration bias, intrinsic alignment and source redshift bias) simultaneously over the ranges given in Table I but combine our measurements with the *Planck* baseline likelihood.<sup>10</sup> In addition, instead of applying Gaussian priors on the shear calibration biases, we vary them over the range  $[-1, 1]$  and evaluate the constraining power that  $w^{\gamma_{t\kappa\text{CMB}}}(\theta)$  has on these parameters.

From this, we obtain  $m^{2,3,4} = [-0.08^{+0.47}_{-0.31}, -0.06^{+0.20}_{-0.28}, -0.14^{+0.14}_{-0.28}]$ . The data does not constrain  $m^1$  well, which could be explained by the small overlap between the CMB lensing and the galaxy lensing kernel for this bin. These results are consistent with the constraints from cosmic shear measurements when the parameters are marginalized over in the same way:  $m^{1,2,3,4} = [0.02^{+0.15}_{-0.16}, -0.04^{+0.09}_{-0.10}, -0.10^{+0.05}_{-0.05}, -0.05^{+0.06}_{-0.06}]$ , but significantly weaker than the imposed priors in [12], which point to best-fit values of  $0.012^{+0.023}_{-0.023}$  for all the bins. These results are summarized in Table III, and the posterior distributions are shown in Fig. 5. Our analysis demonstrates the potential of using cross-correlation measurements between galaxy lensing and CMB lensing to constrain shear calibration bias. However, to reach the level of DES priors, the signal-to-noise of the galaxy-CMB lensing cross-correlations would have to improve by a factor of approximately 30.

<sup>10</sup> Here we use the combination of low- $\ell$  TEB and high- $\ell$  TT likelihoods.

PROBE	$A^{\text{IA}}$
$\gamma_{t\kappa\text{CMB}}$	$0.54^{+0.92}_{-1.18}$
$\gamma\gamma$	$1.02^{+0.64}_{-0.52}$

TABLE IV. Constraints on  $A^{\text{IA}}$  assuming the non-linear alignment model, when combining our  $w^{\gamma_{t\kappa\text{CMB}}}(\theta)$  measurement and the *Planck* baseline likelihood.

### C. Constraining intrinsic alignment parameters

Using the same framework as Sec. VI B we attempt to constrain the non-linear alignment model parameters  $A^{\text{IA}}$  and  $\eta^{\text{IA}}$ . For the amplitude, we obtain  $A^{\text{IA}} = 0.54^{+0.92}_{-1.18}$ , which can be compared to  $A^{\text{IA}} = 1.02^{+0.64}_{-0.52}$ , obtained from the DES-Y1 cosmic shear measurements. These results are in agreement with each other, although it is noted that the values are not well constrained. Since the product of galaxy weak lensing and CMB lensing kernels span a wider redshift range compared to the galaxy weak lensing kernel alone, we might expect to obtain a better constraint on the redshift evolution parameter  $\eta^{\text{IA}}$  using  $\gamma_{t\kappa\text{CMB}}$  correlations over  $\gamma\gamma$ . However, due to the noise level of the CMB lensing map used in this analysis, we find no significant constraint on this parameter. The results are shown in Fig. 5, and are summarized in Table IV.

### D. Cosmological parameter fits

The lensing cross-correlation measurements should be sensitive to the information about the underlying dark matter distribution and the growth of dark-matter structure in the universe, and hence should be sensitive to  $\Omega_m$  and  $S_8 \equiv \sigma_8 \sqrt{(\Omega_m/0.3)}$ . The constraints that we obtain on these parameters are shown in Fig. 6, and are compared with the ones obtained from the DES-Y1 cosmic shear results [11], DES-Y1 joint analysis [12] and CMB lensing alone [10]. The comparison between our results and that of cosmic shear is interesting since we are essentially replacing one of the source planes in [11] with the CMB. We find that the constraints that we obtain for  $w^{\gamma_{t\kappa\text{CMB}}}(\theta)$  are less constraining than but consistent with the cosmic shear results. The marginalized constraints on  $\Omega_m$  and  $S_8$  are found to be  $0.261^{+0.070}_{-0.051}$  and  $0.660^{+0.085}_{-0.100}$  respectively, whereas [11] finds  $\Omega_m = 0.260^{+0.065}_{-0.037}$  and  $S_8 = 0.782^{+0.027}_{-0.027}$ .

## VII. CONCLUSIONS

We have presented a measurement of the cross-correlation between galaxy lensing as measured by DES and CMB lensing as measured by SPT and *Planck*. The galaxy lensing measurements are derived from observed distortions of the images of galaxies in approximately the redshift range of  $0.2 < z < 1.3$ ; the CMB lensing measurements, on the other hand, are inferred from distortions of the CMB temperature map induced by intervening matter along the line of sight of photons traveling from the last scattering surface.

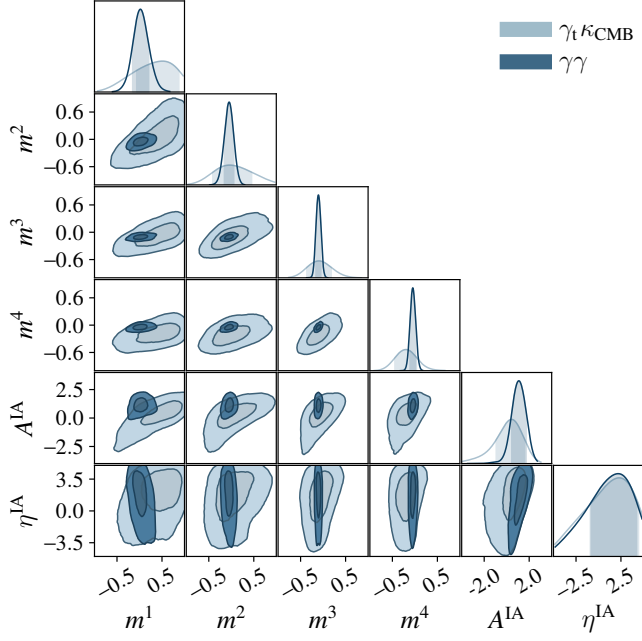


FIG. 5. Constraints on  $m^i$ ,  $A^{IA}$  and  $\eta^{IA}$ , that we marginalize over (source redshift bias parameters are also marginalized over but not shown here). The constraints that we obtain are weaker but in agreement with that from the cosmic shear measurements [11].

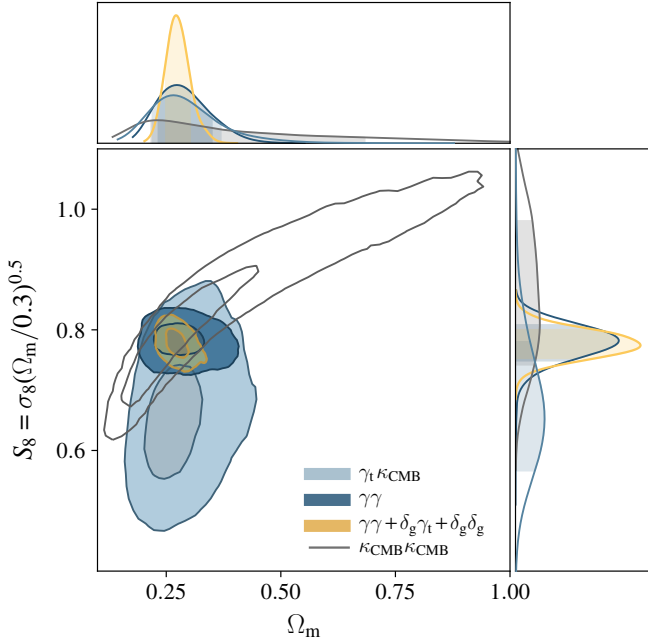


FIG. 6. Constraints on  $\Omega_m$  and  $S_8$  from  $\gamma_t \kappa_{CMB}$ , cosmic shear measurement from [11],  $3 \times 2$ pt measurement from [12] and  $\kappa_{CMB} \kappa_{CMB}$  measurement from [10].

The cross-correlation is detected at  $10.8\sigma$  significance including all angular bins; this is reduced to  $6.0\sigma$  after removing scales that we find to be affected by systematics such as tSZ contamination of  $\kappa_{CMB}$  and the effects of baryons on the matter power spectrum as described in [23].

We perform several consistency checks on the measurements as well as tests for possible systematic errors. These include performing null tests by cross-correlating  $\kappa_{CMB}$  with stellar density, dust extinction, PSF residuals and the cross-shear component, and testing our model for tSZ and CIB contamination of the  $\kappa_{CMB}$  map. We find that of these possible systematics, the tSZ effect dominates, and we mitigate this bias by applying scale cuts to remove the angular scales that are affected the most.

The analytical covariance matrix that we use is tested by comparing with the jackknife covariance matrix estimated directly from the data. The diagonal elements of these covariance matrices agree to within 25%, which is a reasonable agreement given that the jackknife method produces a noisy estimate of the underlying covariance.

Using the measured  $w^{\gamma_t \kappa_{CMB}}(\theta)$  correlation functions, we perform parametric fits. Assuming a  $\Lambda$ CDM *Planck* best-fit cosmology and fixing nuisance parameters to fiducial values set by DES-Y1, we obtain a global best-fit amplitude of  $A = 0.99 \pm 0.17$  which is consistent with expectations from the  $\Lambda$ CDM cosmological model ( $A = 1$ ).

Next, we combine our measurement with the *Planck* baseline likelihood, and vary the nuisance parameters and attempt to constrain them. For the shear calibration bias parameters we obtain the constraints  $m^{2,3,4} = [-0.08^{+0.47}_{-0.31}, -0.06^{+0.20}_{-0.28}, -0.14^{+0.14}_{-0.28}]$ , while  $m^1$  is not constrained well. These constraints are less stringent than the DES-Y1 priors derived from data and simulations, it is anticipated that the  $\gamma_t \kappa_{CMB}$  correlation will be able to constrain shear calibration bias to better precision than these methods [68] for future surveys such as CMB-S4 [69] and LSST [70].

For the amplitude of IA, we obtain the constraint  $A^{IA} = 0.54^{+0.92}_{-1.18}$ , which is in agreement with what is obtained from DES-Y1 cosmic shear measurements. However, the redshift evolution parameter  $\eta^{IA}$  is not constrained well using  $w^{\gamma_t \kappa_{CMB}}(\theta)$  measurement alone.

When we marginalize over the nuisance parameters using the DES-Y1 priors listed in Table I, we obtain constraints on cosmological parameters that are consistent with recent results from [37]:  $\Omega_m = 0.261^{+0.070}_{-0.051}$  and  $S_8 \equiv \sigma_8 \sqrt{\Omega_m/0.3} = 0.660^{+0.085}_{-0.100}$ . While the constraining power of  $\gamma_t \kappa_{CMB}$  is relatively weak, we obtain independent constraints on  $\Omega_m$  and  $S_8$ , which will help break degeneracies in parameter space when all the probes are combined.

Future data from the full DES survey and SPT-3G [71] should provide significant reduction in measurement uncertainties on the  $w^{\gamma_t \kappa_{CMB}}(\theta)$  correlation function. Moreover, tSZ contamination of the temperature-based CMB lensing map necessitates removal of certain angular scales, which reduces the signal-to-noise of the measurements significantly. For SPT-3G, the CMB lensing map will be reconstructed using polarisation data, which will have minimal tSZ contamina-



tion.<sup>11</sup> With these potential improvements, the  $\gamma_t\kappa_{\text{CMB}}$  cross-correlation is a promising probe from which will be used to extract constraints independent of those from galaxy shear or CMB measurements alone.

## ACKNOWLEDGEMENTS

YO acknowledges funding from the Natural Sciences and Engineering Research Council of Canada, Canadian Institute for Advanced Research, Canada Research Chairs program and support from the Kavli Foundation. EB is partially supported by the US Department of Energy grant [de-sc0007901](#). CC was supported in part by the Kavli Institute for Cosmological Physics at the University of Chicago through grant NSF PHY-1125897 and an endowment from Kavli Foundation and its founder Fred Kavli.

Computations were made on the supercomputer Guillimin from McGill University, managed by Calcul Québec and Compute Canada. The operation of this supercomputer is funded by the Canada Foundation for Innovation (CFI), the ministère de l'Économie, de la science et de l'innovation du Québec (MESI) and the Fonds de recherche du Québec - Nature et technologies (FRQ-NT).

This research is part of the Blue Waters sustained-petascale computing project, which is supported by the National Science Foundation (awards OCI-0725070 and ACI-1238993) and the state of Illinois. Blue Waters is a joint effort of the University of Illinois at Urbana-Champaign and its National Center for Supercomputing Applications.

This research used resources of the National Energy Research Scientific Computing Center (NERSC), a DOE Office of Science User Facility supported by the Office of Science of the U.S. Department of Energy under Contract No. DE-AC02-05CH11231.

The South Pole Telescope program is supported by the National Science Foundation through grant PLR-1248097. Partial support is also provided by the NSF Physics Frontier Center grant PHY-0114422 to the Kavli Institute of Cosmological Physics at the University of Chicago, the Kavli Foundation, and the Gordon and Betty Moore Foundation through Grant GBMF#947 to the University of Chicago. The McGill authors acknowledge funding from the Natural Sciences and Engineering Research Council of Canada, Canadian Institute for Advanced Research, and Canada Research Chairs program. CR acknowledges support from a Australian Research Council Future Fellowship (FT150100074) BB is supported by the Fermi Research Alliance, LLC under Contract No. De-AC02-07CH11359 with the United States Department of Energy.

Argonne National Laboratory's work was supported under U.S. Department of Energy contract DE-AC02-06CH11357. Funding for the DES Projects has been provided by the U.S. Department of Energy, the U.S. National Science

Foundation, the Ministry of Science and Education of Spain, the Science and Technology Facilities Council of the United Kingdom, the Higher Education Funding Council for England, the National Center for Supercomputing Applications at the University of Illinois at Urbana-Champaign, the Kavli Institute of Cosmological Physics at the University of Chicago, the Center for Cosmology and Astro-Particle Physics at the Ohio State University, the Mitchell Institute for Fundamental Physics and Astronomy at Texas A&M University, Financiadora de Estudos e Projetos, Fundação Carlos Chagas Filho de Amparo à Pesquisa do Estado do Rio de Janeiro, Conselho Nacional de Desenvolvimento Científico e Tecnológico and the Ministério da Ciência, Tecnologia e Inovação, the Deutsche Forschungsgemeinschaft and the Collaborating Institutions in the Dark Energy Survey.

The Collaborating Institutions are Argonne National Laboratory, the University of California at Santa Cruz, the University of Cambridge, Centro de Investigaciones Energéticas, Medioambientales y Tecnológicas-Madrid, the University of Chicago, University College London, the DES-Brazil Consortium, the University of Edinburgh, the Eidgenössische Technische Hochschule (ETH) Zürich, Fermi National Accelerator Laboratory, the University of Illinois at Urbana-Champaign, the Institut de Ciències de l'Espai (IEEC/CSIC), the Institut de Física d'Altes Energies, Lawrence Berkeley National Laboratory, the Ludwig-Maximilians Universität München and the associated Excellence Cluster Universe, the University of Michigan, the National Optical Astronomy Observatory, the University of Nottingham, The Ohio State University, the University of Pennsylvania, the University of Portsmouth, SLAC National Accelerator Laboratory, Stanford University, the University of Sussex, Texas A&M University, and the OzDES Membership Consortium.

Based in part on observations at Cerro Tololo Inter-American Observatory, National Optical Astronomy Observatory, which is operated by the Association of Universities for Research in Astronomy (AURA) under a cooperative agreement with the National Science Foundation.

The DES data management system is supported by the National Science Foundation under Grant Numbers AST-1138766 and AST-1536171. The DES participants from Spanish institutions are partially supported by MINECO under grants AYA2015-71825, ESP2015-66861, FPA2015-68048, SEV-2016-0588, SEV-2016-0597, and MDM-2015-0509, some of which include ERDF funds from the European Union. IFAE is partially funded by the CERCA program of the Generalitat de Catalunya. Research leading to these results has received funding from the European Research Council under the European Union's Seventh Framework Program (FP7/2007-2013) including ERC grant agreements 240672, 291329, and 306478. We acknowledge support from the Australian Research Council Centre of Excellence for All-sky Astrophysics (CAASTRO), through project number CE110001020.

This manuscript has been authored by Fermi Research Alliance, LLC under Contract No. DE-AC02-07CH11359 with the U.S. Department of Energy, Office of Science, Office of High Energy Physics. The United States Government retains

<sup>11</sup> The lensing potential can also be reconstructed using combinations of temperature maps such that the lensing map is less sensitive to biases; see e.g. [72].



and the publisher, by accepting the article for publication, acknowledges that the United States Government retains a non-exclusive, paid-up, irrevocable, world-wide license to publish or reproduce the published form of this manuscript, or allow others to do so, for United States Government purposes.

We acknowledge the use of many python packages: `ASTROPY`, a community-developed core Python package for Astronomy [73], `CAMB` [30, 54], `CHAIN CONSUMER`<sup>12</sup>, `COSMOSIS`<sup>13</sup>, `HEALPIX` [74], `IPYTHON` [75], `MATPLOTLIB` [76], `NUMPY` & `SCIPLY` [77, 78], `QUICKLENS`<sup>14</sup> and `TREECORR` [79].

- 
- [1] M. Bartelmann and P. Schneider, *Phys. Rep.* **340**, 291 (2001), [astro-ph/9912508](#).
  - [2] L. Fu, E. Semboloni, H. Hoekstra et al., *A&A* **479**, 9 (2008), [arXiv:0712.0884](#).
  - [3] M. J. Jee, J. A. Tyson, M. D. Schneider et al., *Astrophys. J.* **765**, 74 (2013), [arXiv:1210.2732 \[astro-ph.CO\]](#).
  - [4] C. Heymans et al., *Mon. Not. Roy. Astron. Soc.* **427**, 146 (2012), [arXiv:1210.0032 \[astro-ph.CO\]](#).
  - [5] T. Abbott et al. (DES Collaboration), *Phys. Rev. D* **94**, 022001 (2016), [arXiv:1507.05552 \[astro-ph.CO\]](#).
  - [6] M. Kilbinger, *Reports on Progress in Physics* **78**, 086901 (2015), [arXiv:1411.0115](#).
  - [7] M. J. Jee, J. A. Tyson, S. Hilbert et al., *ApJ* **824**, 77 (2016), [arXiv:1510.03962](#).
  - [8] H. Hildebrandt, M. Viola, C. Heymans et al., *MNRAS* **465**, 1454 (2017), [arXiv:1606.05338](#).
  - [9] Planck Collaboration, P. A. R. Ade, N. Aghanim et al., *A&A* **594**, A15 (2016), [arXiv:1502.01591](#).
  - [10] G. Simard, Y. Omori, K. Aylor et al., *ApJ* **860**, 137 (2018), [arXiv:1712.07541](#).
  - [11] M. A. Troxel, N. MacCrann, J. Zuntz et al. (DES Collaboration), *Phys. Rev. D* **98**, 043528 (2018), [arXiv:1708.01538](#).
  - [12] DES Collaboration, T. M. C. Abbott, F. B. Abdalla et al. (DES Collaboration), *ArXiv e-prints* (2017), [arXiv:1708.01530](#).
  - [13] A. J. Benson, S. Cole, C. S. Frenk et al., *MNRAS* **311**, 793 (2000), [astro-ph/9903343](#).
  - [14] N. Hand, A. Leauthaud, S. Das et al., *Phys. Rev. D* **91**, 062001 (2015), [arXiv:1311.6200](#).
  - [15] J. W. Fowler, M. D. Niemack, S. R. Dicker et al., *Appl. Opt.* **46**, 3444 (2007), [astro-ph/0701020](#).
  - [16] T. Erben, H. Hildebrandt, L. Miller et al., *MNRAS* **433**, 2545 (2013), [arXiv:1210.8156](#).
  - [17] J. Liu and J. C. Hill, *Phys. Rev. D* **92**, 063517 (2015), [arXiv:1504.05598](#).
  - [18] D. Kirk, Y. Omori, A. Benoit-Lévy et al. (DES and SPT Collaborations), *MNRAS* **459**, 21 (2016), [arXiv:1512.04535](#).
  - [19] J. Harnois-Déraps, T. Tröster, A. Hojjati et al., *MNRAS* **460**, 434 (2016), [arXiv:1603.07723](#).
  - [20] J. Harnois-Déraps, T. Tröster, N. E. Chisari et al., *ArXiv e-prints* (2017), [arXiv:1703.03383](#).
  - [21] The Dark Energy Survey Collaboration, *ArXiv Astrophysics e-prints* (2005), [astro-ph/0510346](#).
  - [22] Omori, Y. and Giannantonio, T. and Porredon, A. et al., (prep.).
  - [23] E. J. Baxter, Y. Omori, C. Chang et al., *ArXiv e-prints* (2018), [arXiv:1802.05257](#).
  - [24] DES and SPT Collaborations, (prep.).
  - [25] A. Lewis and A. Challinor, *Phys. Rep.* **429**, 1 (2006), [astro-ph/0601594](#).
  - [26] N. Kaiser and G. Squires, *ApJ* **404**, 441 (1993).
  - [27] S. Singh, R. Mandelbaum and J. R. Brownstein, *MNRAS* **464**, 2120 (2017), [arXiv:1606.08841](#).
  - [28] D. N. Limber, *ApJ* **117**, 134 (1953).
  - [29] M. Loverde and N. Afshordi, *Phys. Rev. D* **78**, 123506 (2008), [arXiv:0809.5112](#).
  - [30] A. Lewis, A. Challinor and A. Lasenby, *ApJ* **538**, 473 (2000), [astro-ph/9911177](#).
  - [31] C. Howlett, A. Lewis, A. Hall et al., *JCAP* **4**, 027 (2012), [arXiv:1201.3654 \[astro-ph.CO\]](#).
  - [32] R. E. Smith, J. A. Peacock, A. Jenkins et al., *MNRAS* **341**, 1311 (2003), [astro-ph/0207664](#).
  - [33] R. Takahashi, M. Sato, T. Nishimichi et al., *ApJ* **761**, 152 (2012), [arXiv:1208.2701](#).
  - [34] S. Bird, M. Viel and M. G. Haehnelt, *MNRAS* **420**, 2551 (2012), [arXiv:1109.4416](#).
  - [35] B. Flaugher, H. T. Diehl, K. Honscheid et al. (DES Collaboration), *AJ* **150**, 150 (2015), [arXiv:1504.02900 \[astro-ph.IM\]](#).
  - [36] A. Drlica-Wagner, I. Sevilla-Noarbe, E. S. Rykoff et al., *ApJS* **235**, 33 (2018), [arXiv:1708.01531](#).
  - [37] J. Zuntz, E. Sheldon, S. Samuroff et al. (DES Collaboration), *MNRAS* **481**, 1149 (2018), [arXiv:1708.01533](#).
  - [38] E. Huff and R. Mandelbaum, *ArXiv e-prints* (2017), [arXiv:1702.02600](#).
  - [39] E. S. Sheldon and E. M. Huff, *ApJ* **841**, 24 (2017), [arXiv:1702.02601](#).
  - [40] N. Benítez, *ApJ* **536**, 571 (2000), [astro-ph/9811189](#).
  - [41] B. Hoyle, D. Gruen, G. M. Bernstein et al., *MNRAS* **478**, 592 (2018), [arXiv:1708.01532](#).
  - [42] M. Gatti, P. Vielzeuf, C. Davis et al. (DES Collaboration), *MNRAS* **477**, 1664 (2018), [arXiv:1709.00992](#).
  - [43] C. Davis, M. Gatti, P. Vielzeuf et al. (DES Collaboration), *ArXiv e-prints* (2017), [arXiv:1710.02517](#).
  - [44] C. Laigle, H. J. McCracken, O. Ilbert et al., *ApJS* **224**, 24 (2016), [arXiv:1604.02350](#).
  - [45] Y. Omori, R. Chown, G. Simard et al., *ApJ* **849**, 124 (2017), [arXiv:1705.00743](#).
  - [46] A. van Engelen, S. Bhattacharya, N. Sehgal et al., *ApJ* **786**, 13 (2014), [arXiv:1310.7023](#).
  - [47] T. Okamoto and W. Hu, *Phys. Rev. D* **67**, 083002 (2003), [astro-ph/0301031](#).
  - [48] Z. Hou, K. Aylor, B. A. Benson et al., *ApJ* **853**, 3 (2018), [arXiv:1704.00884](#).
  - [49] J. Prat, C. Sánchez, Y. Fang et al. (DES Collaboration), *ArXiv e-prints* (2017), [arXiv:1708.01537](#).
  - [50] E. Krause, T. F. Eifler, J. Zuntz et al. (DES Collaboration), *ArXiv e-prints* (2017), [arXiv:1706.09359](#).
  - [51] J. Zuntz, M. Paterno, E. Jennings et al., *Astronomy and Computing* **12**, 45 (2015), [arXiv:1409.3409](#).
  - [52] S. Bridle and L. King, *New Journal of Physics* **9**, 444 (2007), [arXiv:0705.0166](#).
  - [53] M. Kilbinger, K. Benabed, J. Guy et al., *A&A* **497**, 677 (2009), [arXiv:0810.5129](#).
  - [54] C. Howlett, A. Lewis, A. Hall et al., *JCAP* **4**, 027 (2012), [arXiv:1201.3654 \[astro-ph.CO\]](#).
- 

<sup>12</sup> <https://samreay.github.io/ChainConsumer>

<sup>13</sup> <https://bitbucket.org/joezuntz/cosmosis>

<sup>14</sup> <https://github.com/dhanson/quicklens>

- [55] D. Kirk, A. Rassat, O. Host et al., *MNRAS* **424**, 1647 (2012), [arXiv:1112.4752](#).
- [56] R. Takahashi, M. Sato, T. Nishimichi et al., *ApJ* **761**, 152 (2012), [arXiv:1208.2701](#).
- [57] S. Joudaki, C. Blake, C. Heymans et al., *MNRAS* **465**, 2033 (2017), [arXiv:1601.05786](#).
- [58] C. Bonnett, M. A. Troxel, W. Hartley et al. (DES Collaboration), *Phys. Rev. D* **94**, 042005 (2016), [arXiv:1507.05909](#).
- [59] M. R. Becker, M. A. Troxel, N. MacCrann et al. (DES Collaboration), *Phys. Rev. D* **94**, 022002 (2016), [arXiv:1507.05598](#).
- [60] E. Rozo, E. S. Rykoff, A. Abate et al., *MNRAS* **461**, 1431 (2016), [arXiv:1507.05460 \[astro-ph.IM\]](#).
- [61] C. Heymans, L. Van Waerbeke, D. Bacon et al., *MNRAS* **368**, 1323 (2006), [astro-ph/0506112](#).
- [62] D. Huterer, M. Takada, G. Bernstein et al., *MNRAS* **366**, 101 (2006), [astro-ph/0506030](#).
- [63] A. Hall and A. Taylor, *MNRAS* **443**, L119 (2014), [arXiv:1401.6018](#).
- [64] M. A. Troxel and M. Ishak, *Phys. Rev. D* **89**, 063528 (2014), [arXiv:1401.7051](#).
- [65] Planck Collaboration, P. A. R. Ade, N. Aghanim et al., *A&A* **594**, A13 (2016), [arXiv:1502.01589](#).
- [66] J. Elvin-Poole, M. Crocce, A. J. Ross et al. (DES Collaboration), *ArXiv e-prints* (2017), [arXiv:1708.01536](#).
- [67] H. S. Xavier, F. B. Abdalla and B. Joachimi, *MNRAS* **459**, 3693 (2016), [arXiv:1602.08503](#).
- [68] E. Schaan, E. Krause, T. Eifler et al., *Phys. Rev. D* **95**, 123512 (2017), [arXiv:1607.01761](#).
- [69] K. N. Abazajian, P. Adshead, Z. Ahmed et al., *ArXiv e-prints* (2016), [arXiv:1610.02743](#).
- [70] LSST Science Collaboration, P. A. Abell, J. Allison et al., *ArXiv e-prints* (2009), [arXiv:0912.0201 \[astro-ph.IM\]](#).
- [71] B. A. Benson, P. A. R. Ade, Z. Ahmed et al., in *Millimeter, Submillimeter, and Far-Infrared Detectors and Instrumentation for Astronomy VII*, Proc. SPIE, Vol. 9153 (2014) p. 91531P, [arXiv:1407.2973 \[astro-ph.IM\]](#).
- [72] M. S. Madhavacheril and J. C. Hill, *ArXiv e-prints* (2018), [arXiv:1802.08230](#).
- [73] The Astropy Collaboration, A. M. Price-Whelan, B. M. Sipőcz et al., *ArXiv e-prints* (2018), [arXiv:1801.02634 \[astro-ph.IM\]](#).
- [74] K. M. Górski, E. Hivon, A. J. Banday et al., *ApJ* **622**, 759 (2005), [arXiv:astro-ph/0409513](#).
- [75] F. Pérez and B. E. Granger, *Computing in Science and Engineering* **9**, 21 (2007).
- [76] J. D. Hunter, *Computing In Science & Engineering* **9**, 90 (2007).
- [77] E. Jones, T. Oliphant, P. Peterson et al., “SciPy: Open source scientific tools for Python,” (2001–).
- [78] T. E. Oliphant, *Guide to NumPy*, 2nd ed. (CreateSpace Independent Publishing Platform, USA, 2015).
- [79] M. Jarvis, “TreeCorr: Two-point correlation functions,” *Astro-physics Source Code Library* (2015), [ascl:1508.007](#).

## Appendix A: Flask simulations

In this work, we make use of the publicly available code FLASK [67], to generate correlated maps between shear and CMB lensing. We use FLASK to generate 120 full-sky log-normal realizations of the density field and four galaxy shear maps corresponding to the four redshift bins we use for the data. Additionally, we generate a convergence map at  $z = 1089$ , and treat this as a noiseless CMB convergence map.

The galaxy shear catalogs are generated using galaxy number densities and shape noise measured from data, and Gaussian noise realizations generated from the noise power spectrum of the CMB convergence maps are added to the noiseless convergence map to produce data-like catalogs and maps. For each full sky simulation, we extract out ten sub-catalogs by applying the DES-Y1 angular mask, resulting in 1200 synthetic galaxy shear catalogs and CMB convergence maps that have noise properties matched to the real data.

## Appendix B: Validation of jackknife covariance estimate

To test whether the jackknife covariance estimate provides a reliable estimate of the true covariance over the scales considered, we make use of FLASK simulation realizations. For each of the simulated catalogues, we measure  $w^{\gamma_l K_{\text{CMB}}}(\theta)$  using the same procedure as applied to the real data. We then compute the covariance matrix directly across the 1200 simulated catalogs, which provides a low-noise estimate of the covariance of  $w^{\gamma_l K_{\text{CMB}}}(\theta)$  in the FLASK simulations. (which we call “true” FLASK covariance). From the simulated catalogue, we also compute the jackknife estimate of the covariance and compare this with the true FLASK covariance. We find that these are consistent with each other to within 25%.